Clim. Past Discuss., 8, 4885–4922, 2012
www.clim-past-discuss.net/8/4885/2012/
doi:10.5194/cpd-8-4885-2012

Climate of the Past Discussions

Variations of oceanic oxygen isotopes at the present day and the LGM: equilibrium simulations with an oceanic general circulation model

X. Xu, G. Lohmann, M. Werner, and X. Zhang

Alfred Wegener Insitute for Polar and Marine Research, Bremerhaven, Germany

Received: 15 August 2012 – Accepted: 21 September 2012 – Published: 1 October 2012

Correspondence to: X. Xu (xu.xu@awi.de)

Published by Copernicus Publications on behalf of the European Geosciences Union.

Abstract

The isotope-enabled oceanic general circulation model, MPI-OM, is used to simulate the oxygen isotope compositions of sea waters in the oceans under preindustrial and last glacial maximum climate conditions. Simulated oceanic isotope distributions at the last glacial maximum (21 000 yr ago) show features similar to the preindustrial in most basins but the Northern North Atlantic. With the exception of the ice sheet impact, the oxygen-18 content variations at sea surface during the last glacial maximum are mainly controlled by the changes in boundary isotopic fluxes in most regions, while the changes from subsurface to bottom waters are mostly due to the differences in the water mass circulations. The changes in topography at the northern high latitudes have a remarkable influence on the isotopic composition in the Arctic Ocean. The pre-industrial and the last glacial maximum calcite oxygen isotope compositions in the surface water and their difference are also calculated. These results are compared with the observed values from different foraminifera species and are in agreement with the observations in most regions.

1 Introduction

Analysis of oxygen isotopes in foraminiferal calcite has been applied in most oceanic paleoclimate studies after the first measurements were made in 1950s (Emiliani, 1955). The variations of calcite oxygen isotope content in sediment cores (typically expressed in a delta notation as $\delta^{18}O_c$) provide quantitative interpretation of past climate changes. Since the oxygen isotope composition of marine in carbonate is mainly dependent on both the oxygen isotope content and temperature of the ambient water (Urey, 1947), many empirically derived paleotemperature equations (Epstein et al., 1953; Craig, 1965; O'Neil et al., 1969; Shackleton, 1974; Erez and Luz, 1983; Bemis et al., 1998; Mulitza et al., 2003) have been published during the past several decades. These relations are used to constrain the past sea surface temperature by employing the

CPD
8, 4885–4922, 2012

measured $\delta^{18}O_c$ from planktic foraminifera (Broecker, 1986; Zachos et al., 1994; Meland et al., 2005). In these applications, changes of the oxygen isotope ratio in sea water ($\delta^{18}O_w$) are either estimated by the global ice volume effect or by the implementation of an empirical relationship (e.g. between $\delta^{18}O_w$ and salinity) reflecting the modern water isotope variability. However, local variations of oxygen isotope in sea water are affected by multiple factors (global ice volume, isotopic fluxes, and ocean circulation), which can all differ from present day. An isotope-enhanced climate model is therefore needed to acquire the sea water isotopic distribution under paleo-climate conditions. This modelling approach also enables the evaluation of the simulated climate condition by direct comparison between modelled and observed oxygen isotope composition in planktic foraminifera (Schmidt, 1999; Roche et al., 2004; Tindall et al., 2010).

In the present study, the stable oxygen isotope ratio in sea water ($\delta^{18}O_w$) and foraminiferal calcite ($\delta^{18}O_c$) are simulated in an isotope-enhanced oceanic general circulation model under both the present-day (PD) and last glacial maximum (LGM) conditions. The model results are discussed for different oceanic basins to understand the processes that lead to the isotopic distribution of oxygen-18 at the sea surface and in the deep water. Sensitivity studies are used to understand the factors giving rise to the variations of $\delta^{18}O_w$ during PD and LGM. A comparison of the modelled $\delta^{18}O_c$ distribution at the sea surface with available planktonic foraminifera observations at PD and LGM examines the model performance in capturing the main characteristics of oceanic changes during PD and LGM.

2 Methods

2.1 Model description

We use the oceanic general circulation model MPIOM-wiso (Xu et al., 2012) for long-term simulations under the PD and LGM conditions. MPIOM-wiso is a derivative of the

CPD
8, 4885–4922, 2012

Max-Planck-Institute Global Ocean/Sea-Ice Model (Marsland et al., 2003) enhanced by explicit water isotope diagnostics. Water isotopes, $H_2{}^{16}O$ and $H_2{}^{18}O$, are implemented as passive tracers in terms of mass in MPIOM-wiso, and the isotope value is described in a permil-based delta notation (δ). The isotopic variations occurring in MPIOM-wiso primarily depend on the isotopic composition of freshwater fluxes at the ocean surface (evaporation and precipitation), the isotope content of river discharge, and the oceanic advection and mixing of different water masses. The river runoff is calculated from the continental net precipitation based on the assumption that the global water cycle is balanced.

In this study, changes of oxygen isotopes occurring at phase transitions of water during the formation of sea ice are also included. Because sea ice formation is assumed to occur at isotopic equilibrium, the isotopic composition of sea ice is calculated by a liquid to ice fractionation factor. For our experiments, this fractionation factor is set to 1.003, which is the average from various estimates (Craig and Gordon, 1965; Majoube, 1971; Lehmann and Siegenthaler, 1991; Macdonald et al., 1995). There is no fractionation accompanied during sea ice melting due to the very low rate of isotopic diffusion in sea ice.

2.2 Experimental setup

The ocean model is configured with a formal horizontal resolution of $3^\circ \times 1.8^\circ$ and 40 unequal vertical layers. Poles are on Greenland and Antarctic, respectively. For the present-day experiment, the ETOPO-5 data set (data announcement 88-MGG-02, digital relief of the surface of the Earth NOAA, National Geophysical Data Center, Boulder, Colorado, 1988) is used to create the grid-based topography and bathymetry. In the LGM simulations, the mean sea level is lowered by 116 m corresponding to the glacial ice-sheet extent, in agreement with the settings of the Paleoclimate Modelling Intercomparsion Project Phase III (PMIP3, https://pmip3.lsce.ipsl.fr/). Therefore, the Hudson Bay and the Barents Sea are covered by the main Northern Hemisphere ice sheets, and the Bering Strait is closed.

CPD
8, 4885–4922, 2012

Initial conditions for marine temperature and salinity in the PD simulation are interpolated from climatological fields (Steele et al., 2001). Initialization of potential temperature and salinity for the LGM run stem from an LGM simulation of the Earth System Model COSMOS (Zhang et al., 2012). Sea surface salinity is restored with a time scale of 39 days in both the PD and LGM experiment.

For the initial distribution of $H_2{}^{18}O$ in the present-day ocean, a homogenous setup has been chosen with all isotope values set to present-day $\delta^{18}O_w$ values of 0 ‰ with reference to the Vienna Standard Mean Ocean Water (Baertschi, 1976). In accordance with the larger ice sheet volume at LGM, 1 ‰ is added to the LGM $\delta^{18}O_w$ initial distribution (Schrag et al., 2002). No surface restoring of water isotopes is applied.

Both the PD and LGM simulations have been run for 3000 yr into a quasi-steady state. For the analyses we used the mean state of the last 100 simulation years.

2.3 Atmospheric and isotopic forcing

The atmospheric forcing for PD and LGM conditions are derived from the atmospheric general circulation model ECHAM5-wiso in a T31 spectral resolution (about $3.75^\circ \times 3.75^\circ$) with 19 vertical levels (Werner et al., 2011). Mean daily values of heat, freshwater and momentum fluxes at the air-sea interface are obtained from a 10 yr simulation period. For PD, AMIP-conform (Gates et al., 1999) present-day boundary conditions, including monthly climatological sea surface temperatures and sea ice cover of the period 1979–1999 have been prescribed. For LGM, ECHAM5-wiso used SST and sea ice boundary conditions calculated from the difference between a PD and a LGM simulation employing the climate model COSMOS under present and glacial conditions (Zhang et al., 2012). The glacial simulations use the community earth system models (COSMOS, version: COSMOS-landveg r2413, 2009) which have been mainly developed by the Max Planck Institute for Meteorology (MPI) in Hamburg. The setup is identical to the COSMOS-1.2.0 release, that has been developed in the Millennium project (Jungclaus et al., 2010), but additionally includes a dynamical vegetation module (Brovkin et al., 2009). Other paleoclimatological studies that employed the

CPD
8, 4885–4922, 2012

same setup comparable to the one used here have successfully been applied for the Holocene (Fischer and Jungclaus, 2010; Wei et al., 2012; Wei and Lohmann, 2012; Varma et al., 2012), the Pliocene (Stepanek and Lohmann, 2012), and the Miocene (Knorr et al., 2011).

In order to ensure maximum consistency between the prescribed climatological forcing and the related isotopic fluxes, the daily isotopic content of precipitation and evaporation fluxes over ocean surfaces stem from the same PD and LGM ECHAM5-wiso simulations which are used for obtaining the default freshwater, heat and momentum flux forcing.

In a sensitivity experiment, we set all boundary conditions like for the LGM simulation, except for the daily isotopic forcing, which was set to the PD values. This sensitivity experiment is named as ISOPD hereafter. It will allow us to distinguish between the impact of LGM ocean circulation changes and glacial isotopic changes in the precipitation and evaporation fluxes on the simulated isotopic composition of ocean water masses.

2.4 Observational database of $\delta^{18}O_c$

For the late Holocene, a global planktic foraminifera oxygen isotope data set has been assembled within the MARGO project (Waelbroeck et al., 2005). Assuming that late Holocene and present-day conditions of the oceans are very similar, we use this data set to evaluate our PD simulation. The data set is composed of over 2100 records from recent sediments with thorough age control that have been checked for internal consistency.

The LGM observational data consists of glacial sediments in the MARGO oxygen isotope dataset (Kucera et al., 2005a), Coral Sea sediments (Anderson et al., 1989), Western Pacific sediments (Martinez et al., 1997), as well as North Atlantic/Nordic Sea sediments (Meland et al., 2005).

CPD
8, 4885–4922, 2012

3 Results

3.1 Comparison of simulated LGM and PD ocean

First we present the sea surface temperature (SST) and sea surface ice concentration (SIC) of the LGM simulation and then compare them with the present day results. The global mean SST in LGM is approximately 2.8 °C colder than present day. As illustrated in Fig. 1, the tropical regions are about 3 to 4 °C colder at LGM as compared to present day, and the SST gradient pattern in tropical and sub-tropical regions are similar to present day. Distinct features are found in mid-to-high latitudes in both hemispheres, especially in the North Atlantic. The most pronounced SST decrease is located in the eastern basin of the Nordic Seas and off the eastern coast of the Laurentide ice sheet, where the cooling is more than 6 °C. In the Southern Ocean, an annular cooling pattern is simulated with a strong cooling at around 40°–45° S. In the Arctic Ocean and south of 65° S, there is not much difference between LGM and present day SST due to the permanent sea ice cover at both LGM and present day at these regions.

In response to the cold climate at LGM, the sea-ice extents reach lower latitudes in both hemispheres compared with the PD simulation (Fig. 1b). The sea ice extent changes are in agreement with the SST differences between LGM and PD at high latitudes. Few variations (< 10 %) are found in the regions, which exhibit permanent sea ice cover at present day. In our simulation, the increase in sea ice compactness in the Eastern Nordic Seas is up to 90 %. There is also noticeable SIC increase around the coast of Newfoundland extending far into the Western Atlantic. The LGM sea ice coverage extends further north in the Southern Ocean compared with the PD conditions (Fig. 1b).

The Atlantic meridional overturning circulation (AMOC) is one of the most important features for examining the large-scale ocean circulation. As shown in Fig. 2, the main difference between the LGM and PD AMOC is in the characteristics of their upper cell. At LGM, the upper cell of AMOC is around 400–500 m shallower than present day. The maximum value of this cell is centered at around 1 km at both LGM and present day,

CPD
8, 4885–4922, 2012

and it is slightly weaker at the LGM. Remarkable decrease in the strength of the AMOC occurs at 2 km depth, where the circulation is reduced by 4 to 5 Sv at LGM. The lower cell of the AMOC is located slightly upward at the LGM and is relatively stronger due to the more pronounced antarctic bottom water.

3.2 Simulated $\delta^{18}O_w$ distributions and LGM-PD comparison

Modelled isotopic distribution in LGM, PD, and ISOPD simulations present the behavior of oceanic oxygen isotope composition under different scenarios of ocean circulation and isotopic fluxes. First we evaluate the sea surface zonal-mean isotopic compositions in the modelled results. As illustrated in Fig. 3, the LGM and ISOPD experiments simulate higher $\delta^{18}O_w$ values at most latitudes than the PD results, which predominantly fall within the range of −3 ‰ to +1.5 ‰ and −4 ‰ to +2 ‰, respectively. In general, the variation of $\delta^{18}O_w$ south of 30° N as modelled by ISOPD is almost parallel to the PD distribution. The LGM $\delta^{18}O_w$ also falls within the range of the other two simulations south of 30° N, but exhibits slightly higher values in the Southern Ocean. In both LGM and ISOPD results, the largest deviations from PD are found in northern mid-to-high latitudes, where an abrupt increase in $\delta^{18}O_w$ occurs around 60° N followed by a sharp decrease. Despite the increase around 60° N, similar to PD the simulated LGM $\delta^{18}O_w$ obeys the latitudinal decrease trend that mainly results from the temperature decrease. The slight enrichment of the water isotope composition in the subtropics in comparison to the equatorial regions indicates relative excess in evaporation over subtropical oceans at the LGM. The most enriched area, both at the LGM and present day, is located around 30° N. The zonal mean LGM $\delta^{18}O_w$ values reach almost +1.6 ‰ there. At the LGM, the most depleted regions are found north of 75° N, with $\delta^{18}O_w$ values less than −2 ‰.

For further illustration, the simulated global $\delta^{18}O_w$ distributions at the sea surface under LGM, PD, and ISOPD boundary conditions are shown in Fig. 4. With the exclusion of the additional glacial +1 ‰ prescribed $\delta^{18}O_w$ in the initial isotopic conditions

CPD
8, 4885–4922, 2012

(for LGM and ISOPD, only), there are no substantial changes of isotopic spatial patterns simulated for the LGM climate, especially at mid-to-low latitudes. In the LGM results, the Atlantic Ocean between 30° S and 40° N shows much enriched isotopic values, especially in the Northern Hemisphere ($\delta^{18}O > 1.5$‰), in contrast to the Pacific Ocean. The northward transport of these enriched waters by the North Atlantic Drift only reaches the Greenland Sea, while in the PD run they approach further north. Extremely depleted values are seen in the marginal areas of the Arctic Ocean (−4‰ to −8‰, Fig. 4).

The surface $\delta^{18}O$ distributions in LGM and ISOPD display rather similar characteristics. The enriched surface water is mainly located in tropical to subtropical region in both cases, but these waters are more enriched in the ISOPD simulation than in the LGM one. The isotope values in the Arctic Ocean under the present day isotopic forcing are more depleted and homogenous. In addition, the depleted Pacific eastern boundary is more pronounced in the LGM simulation than in the ISOPD experiment. In general, estuaries constitute the most depleted regions because of the influx of depleted waters discharged by rivers.

In order to further examine the isotopic changes due to the hydrological variations at the LGM, the $\delta^{18}O_w$ differences between LGM and ISOPD, between ISOPD and PD, as well as the anomaly between LGM and PD (Fig. 5) are calculated. In these calculations, the additional 1‰ is also subtracted from the ISOPD-PD and LGM-PD differences. Under the LGM ocean circulation condition, the differences introduced by the isotopic fluxes in the Southern Ocean and the India Ocean are around ±0.2‰ (Fig. 5a). The depletion in the (sub-)tropical Atlantic Ocean (< −0.4‰) is less than in the Pacific Ocean (up to −0.8‰) due to the isotopic fluxes. Noticeable increase in $\delta^{18}O$ values are found in the Arctic Ocean and the Baffin Bay, where the anomalies are more than +1‰. If we prescribe present-day isotopic composition of precipitation and evaporation, the LGM changes in circulation and topography result in greater variations north of 30° N (> ±0.4‰, Fig. 5b). The $\delta^{18}O$ values in the Northern North Pacific are around −0.6‰ lower under the LGM circulation, and the North Atlantic Drift is slightly

CPD
8, 4885–4922, 2012

enriched (∼ 0.2 ‰). The LGM circulation and river runoff cause strong depletion (more than −2 ‰) in the Arctic Ocean. Combining the fluxes and circulation factors (Fig. 5c), the sea surface isotopic composition at LGM is more depleted by up to −1 ‰ in most basins when compared with PD. Significant decrease is seen in the Arctic Ocean, where $\delta^{18}O$ values are around 1 ‰ to 2 ‰ lower compared with present day. In the Labrador Sea and the Baffin Bay, there is a distinct increase in $\delta^{18}O$ values, where the isotopic enrichment rises by up to +2 ‰. In the Northern Atlantic, slight enrichment is shown between 45° N and 60° N. These depletions are much less in the Southern Atlantic and Indian Oceans, where the anomalies range between −0.2 ‰ and 0 ‰. In contrast to northern high latitudes, the Southern Ocean is slightly enriched during LGM.

The same set of analyses is applied to the subsurface and deep waters in the Atlantic and Pacific Oceans. As seen in Fig. 6, a meridional cross-section of LGM $\delta^{18}O_w$ values in the Atlantic basin reveals a similar pattern as seen in the PD simulation, but shallower $\delta^{18}O_w$-enriched waters are found in the North Atlantic. The enriched North Atlantic surface water that sinks to about 1 km water depth makes the most enriched water mass in the Atlantic section. Below 2.5 km, the comparably depleted antarctic bottom water dominates. The vertical isotopic patterns in the Atlantic are quite alike in the LGM and ISOPD simulation and only slight differences in the $\delta^{18}O_w$ values can be seen in the enriched upper branch and the depleted lower branch. Differences are depicted in greater detail in Fig. 7. In comparison to the modern isotopic fluxes, the LGM conditions show slightly depleted (∼ −0.1 ‰) waters from the surface to 2 km depth, where the North Atlantic Deep Water (NADW) dominates. The bottom water, which originates from the Southern Ocean, however, is around 0.2 ‰ enriched under the LGM isotopic forcing. The result of the ISOPD experiment for the Atlantic cross-section is also compared with the PD simulation. In this case, the changes of the vertical isotopic distribution are reversed. The LGM circulation enriched most of the NADW by around 0.1 ∼ 0.2 ‰, but the $\delta^{18}O_w$ values in the bottom water show a decrease of approximately 0.4 ‰. In general, the variations in the Atlantic subsurface and deep waters

CPD
8, 4885–4922, 2012

due to the changes of isotopic boundary conditions and circulation are smaller (−0.3 ‰ to +0.3 ‰) when compared with the assumed total glacial ice volume effect (+1 ‰).

The isotopic distribution in the Pacific section is distinct from the Atlantic basin (Fig. 8). In the LGM simulation, a relatively enriched water mass originates from 40° S–20° S and has a subsurface extension up to the equator. There is a clear branch of relatively depleted water starting from north of 40° N that sinks to 1 km. The isotopic composition in the Pacific basin is lower than in the Atlantic basin at the LGM. The ISOPD results present almost the same distribution as seen in the LGM simulation, but more enriched subsurface water. In these two cases, the depletion of bottom water is pronounced. Comparisons between the different simulations are illustrated in Fig. 9. The variations along the Pacific basin are well stratified in the LGM-ISOPD comparison. The LGM isotopic forcing produces more depleted waters in the upper 1.5 km. The changes in the $\delta^{18}O_w$ values vary from −0.1 ‰ to −0.4 ‰ between surface and 1.5 km depth. Below 1.5 km, the $\delta^{18}O_w$ values are slightly higher (+0.1 ‰ to +0.2 ‰), with a clear origin of these enriched water masses in the Southern Ocean. From the ISOPD-PD comparison, we infer that the ocean circulation under the LGM climate condition leads to a depletion at most depths. Only the subsurface waters at tropical and subtropical regions are slightly enriched (+0.1 ‰). The decreases in the $\delta^{18}O_w$ values in the Southern Ocean are up to −0.4 ‰. There is a distinct depleted tongue that originates in the North Pacific Ocean, and penetrates southward. The isotopic fluxes and circulation effects together make a large depletion in the upper North Pacific, but compared with PD the variations in most areas at LGM are less than −0.2 ‰.

3.3 Variations of $\delta^{18}O_c$ at LGM and PD

Using the SST and $\delta^{18}O_w$ values from the PD and LGM simulation, we simulate the zonal mean sea surface $\delta^{18}O_c$ at present day and LGM (Fig. 10) by applying the following empirical "paleo-temperature" equation (Shackleton, 1974):

$$\delta^{18}O_c = 21.9 + \delta^{18}O_w - \sqrt{310.61 + 10 \cdot T}$$

CPD
8, 4885–4922, 2012

where T is in °C. In Fig. 10a, the modelled $\delta^{18}O_c$ at the ocean surface and the bottom of the euphotic zone at approx. 100 m (equal to the 8th model layer in MPI-OM) in the present day simulation are compared with a recent compilation of late Holocene $\delta^{18}O_c$ data from different foraminiferal species (Waelbroeck et al., 2005). The modelled annual zonal mean $\delta^{18}O_c$ values ranges from −4 ‰ to 4 ‰ in the upper ocean with low values at tropical to subtropical latitudes and high values at high latitudes. In general, the simulated $\delta^{18}O_c$ values from the PD simulation resemble the measured $\delta^{18}O_c$ distribution. Considering the longitudinal variability in modelled surface $\delta^{18}O_c$, most late Holocene data lie within the spread (shaded area).

For the LGM, the general trend of zonal mean $\delta^{18}O_c$ mirrors the present day simulation, with $\delta^{18}O_c$ values increasing towards high latitudes. The simulated $\delta^{18}O_c$ values vary between −2 ‰ and +6 ‰ (with the global ice sheet effect of +1 ‰ included). But an abrupt decrease occurs around 60° N in the LGM simulation, which is absent in the PD experiment. In general, the LGM $\delta^{18}O_c$ values are higher than the present-day ones, indicating a colder climate during LGM. The simulation results are comparable with the observational data from LGM sediment cores, especially in tropical to subtropical areas. Most data are within the range of $\delta^{18}O_c$ estimated by the model (shaded area). The largest model-data difference is located in high northern latitudes, where the simulated abrupt LGM $\delta^{18}O_c$ depletion is absent from the observations.

In order to examine the model simulation in more detail, a cell-by-cell comparison between observations and model results is made. All observations within a specific grid cell are averaged and compared with the corresponding MPIOM-wiso result. Figure 11 shows the comparison for different planktic foraminifera species for the PD simulation. Most of the results scatter around the 1 : 1 lines, with a slight upper shift for all species. The correlation (*G. ruber*: 0.91, *G. sacculifer*: 0.82, *G. bulloides*: 0.84, *N. pachyderma*: 0.67) and normalized root mean square errors NRMSE (*G. ruber*: 14.0 %, *G. sacculifer*: 15.7 %, *G. bulloides*: 15.4 %, *N. pachyderma*: 22.0 %) between model results and observations indicate a good and significant agreement between them. Except *N. pachyderma* ($r = 0.77$ at 100 m depth), other species exhibit a higher correlation

CPD
8, 4885–4922, 2012

between model and observation at the surface layer than the 100 m depth. The same analyses are applied to the LGM simulation to test the correspondence between the modeled and observed glacial $\delta^{18}O_c$ values. As shown in Fig. 12, the simulated $\delta^{18}O_c$ values for *G. ruber*, *G. sacculifer*, and *N. pachyderma* are comparable with the observations. They are well correlated with the sediment data (*G. ruber*: 0.90, *G. sacculifer*: 0.82, *N. pachyderma*: 0.71), and the corresponding NRMSE are 16.3 %, 23.4 %, and 22.4 %, respectively. For *G. ruber* and *N. pachyderma* most simulated $\delta^{18}O_c$ values are relatively higher than the observed values. The highest $\delta^{18}O_c$ values reach up to +6 ‰ in the simulation for *N. pachyderma*, while the observation range between +3 ‰ and +5 ‰. As with the present day simulation, only *N. pachyderma* shows a slightly higher correlation (0.73) at 100 m depth. For *G. bulloides* the deviations between observed and modelled $\delta^{18}O_c$ values show a larger spread with a NRMSE of 35 % than for the other foraminifera species.

Next, we compare the simulated LGM-PD $\delta^{18}O_c$ differences with the observations. Because the main LGM observations are located in tropical to subtropical regions and the Northern North Atlantic, we only show the LGM-PD $\delta^{18}O_c$ differences between 40° S and 40° N (Fig. 13), as well as north of 40° N in the North Atlantic (Fig. 14). *G. ruber*, *G. sacculifer*, and *G. bulloides* are used to evaluate the modelled $\delta^{18}O_c$ differences between 40° S and 40° N, while *N. pachyderma* $\delta^{18}O_c$ changes depict the variations north of 40° N in the Atlantic. Again, all $\delta^{18}O_c$ differences derived from different observations within a specific grid cell are averaged for this comparison.

As seen in Fig. 13, the simulated $\delta^{18}O_c$ differences between LGM and PD vary from +1 ‰ to +2 ‰ in tropical to subtropical ocean (the ice sheet effect is included), and most values fall into the range +1.4 ‰ to +1.8 ‰. For all foraminifera species shown in Fig. 13, our model results agree with the majority of observations, and the slight overestimate of $\delta^{18}O_c$ in the simulation is less than 0.2 ‰ in most areas. Distinct disagreement between model results and measurements is seen in the South China Sea, where the observed increase in $\delta^{18}O_c$ (> 1.4 ‰) is more pronounced than the simulated changes (< 1 ‰).

CPD
8, 4885–4922, 2012

In the Northern North Atlantic, the largest glacial increase in $\delta^{18}O_c$ (> 3 ‰) occurs at strongly cooled regions as seen in Fig. 1. The simulated LGM-PD $\delta^{18}O_c$ differences in most regions agree reasonable well with the observations. Our model simulates a larger increase in $\delta^{18}O_c$ in the Eastern Nordic Sea as compared with the western basin, which is also in agreement with the observations. But the model results show a decrease in $\delta^{18}O_c$ along the Eastern Greenland Current and north of 80° N, which deviates from the measurements.

4 Discussions

In our LGM results, a substantial cooling of the global oceans occurs. Compared to present day, the decrease of global mean sea surface temperature (SST) is analogous to glacial SST changes estimated from proxy data (MARGO, 2009). The strong thermal gradient in the Northern Hemisphere is well simulated at around 40–45° N. Another region of strong decrease in temperature that extends from the eastern of Iceland to the Eastern Nordic Sea is comparable to the paleo-reconstruction (de Vernal et al., 2006; Kucera et al., 2005b). In our simulation, a segment of ocean in the east of the Nordic Sea is perennially frozen; this region is indicated as sea-ice free area in GLAMAP and some recent reconstructions (Kucera et al., 2005b; de Vernal et al., 2006). In general, previous reconstructions suggest a 0–3 °C decrease in most tropical regions during LGM (Ballantyne et al., 2005; Barrows and Juggins, 2005; Waelbroeck et al., 2009), our model results (3–4 °C) overestimate this tropical cooling. In the southern oceans, the strong cooling around 45° S indicates a northward shift of the polar front during the LGM, increasing the extent of sea-ice concentrations in the Southern Ocean (Gersonde et al., 2005).

Different model studies have produced widely different Atlantic glacial circulation scenarios. Some studies show a stronger and slightly deeper overturning cell (Kitoh et al., 2001) or uniform vertical extent (Hewitt et al., 2003) while others show a weaker and shallower overturning (Shin et al., 2003; Otto-Bliesner et al., 2006). In response to the

CPD
8, 4885–4922, 2012

simulated hydrological conditions, the behavior of the AMOC in our MPI-OM LGM simulation generally agrees with a robust AMOC scenario, which is constrained by observations (Lynch-Stieglitz et al., 2007). Therefore we rate our modelled LGM simulation results as a reasonable glacial circulation, suitable for our isotope studies.

The variation of the surface $\delta^{18}O_w$ distribution during LGM is mainly caused by the change in continental ice storage and atmospheric isotope fluxes at the air–ocean interface (Juillet-Leclerc et al., 1997). Since we prescribe this ice sheet effect in our experiment, the variation in the model results mainly represent the local changes introduced by the different surface isotope fluxes and the glacial ocean circulation.

During the LGM, the influences from the surface fluxes and the circulation vary in different regions. The LGM surface isotope distributions in the Pacific and in the (sub)tropical Atlantic (40° S–40° N) are similar to modern conditions, which suggests comparable surface current pattern in these regions in the two climate states. This result is in agreement with proxy reconstructions (Ortiz et al., 1997; LeGrande and Schmidt, 2006) and other model simulations (Clauzet et al., 2007). Therefore the simulated changes of surface $\delta^{18}O_w$ in these areas are dominated by the glacial variations in the isotopic fluxes. The decrease in $\delta^{18}O_w$ is possibly due to less evaporation during the LGM, which is consistent with the lower surface temperatures during glacial climates. In contrast, the significant changes in the topography and surface currents in the Northern North Atlantic and northern polar region overwhelm the influences introduced by the surface fluxes. During the LGM, the closed Canadian Arctic Archipelago prevents the depleted Arctic water from entering Baffin Bay, which induces a further enrichment of Baffin Bay and Labrador Sea water masses. As a consequence, the Labrador Current brings relatively enriched $\delta^{18}O$ water to the Atlantic. The North Atlantic Current has only a narrow northeasterly branch (Watkins et al., 2007) feeding the enriched waters to the Eastern Nordic Seas. The glacial northward transport of enriched waters into the polar region is therefore much weaker than the present one. In addition, the presence of large ice sheets over North America and North Europe at the LGM had a strong impact on the river pathways and their discharge into the

CPD
8, 4885–4922, 2012

Arctic Ocean (Alkama et al., 2008). These changes enabled a strongly depleted river discharge to reach the Central Arctic, which in combination with the weak northward transport of enriched water masses produced highly depleted surface waters in the Arctic during the LGM.

In contrast to the surface ocean, the variation of the vertical $\delta^{18}O_w$ distribution is mainly caused by the different meridional overturning circulation during the LGM. The isotope distribution in the Atlantic section is in line with the AMOC condition at the LGM. In the North Pacific, there is a zone of intense subsurface water formation, possibly due to a relatively strong cooling in that area. Overall, in most regions the simulated isotopic variations caused by the changes in glacial surface isotope fluxes and ocean circulation are less than the estimated global mean ice sheet impact of +1 ‰, especially in the deep oceans.

No direct measurements of the LGM sea surface waters' isotopic composition exist, which makes it difficult to validate the related model results. However, the simulated calcite $\delta^{18}O_c$ values derived from the modelled sea surface temperature and $\delta^{18}O_w$ values enable a detailed model-data comparison. As seen in the results, the surface $\delta^{18}O_c$ distributions derived from the MPIOM-wiso model are consistent with the $\delta^{18}O_c$ measurements at both present day and glacial time. The simulation for (sub)tropical regions agree with $\delta^{18}O_c$ measurements from *G. ruber* and *G. sacculifer* in both zonal mean and cell-to-cell comparisons for the PD and LGM simulation. At high latitudes, the slight upper shift of the model-data scatter plot for *N. pachyderma* in the present-day comparison indicates a bit lower sea surface temperature at these regions in our PD simulation. Extremely high $\delta^{18}O_c$ values (> 6 ‰) are mainly simulated in the Eastern Nordic Sea at LGM, which is approximately 1 ‰ higher than the observed $\delta^{18}O_c$ of *N. pachyderma*. This overestimate may indicate colder sea surface temperatures in our LGM simulation than the real glacial conditions in the Eastern Nordic Sea. For *G. bulloides*, many LGM measurements are obtained from coastal upwelling regions, which are not well captured by the model simulation. This may be the reason for the large divergence in *G. bulloides* $\delta^{18}O_c$ between the LGM simulation and the measurements.

CPD
8, 4885–4922, 2012

As an increase of $\delta^{18}O_w$ enhances the oxygen isotope composition in the foraminiferal calcite, the simulated decrease in $\delta^{18}O_w$ due to the glacial boundary condition and circulation dampens the positive ice sheet effect of $\delta^{18}O_w$. As a consequence, in those (sub)tropical regions, where the isotopic forcing and circulation conditions have a strong impact on the sea surface isotope composition, the overall glacial increase in $\delta^{18}O_c$ is relatively small. In general, the simulated $\delta^{18}O_c$ increase at the LGM is only slightly higher than the observations, which may indicate a small overestimation of the simulated tropical sea surface cooling. In the Eastern Nordic Sea, although the modelled LGM $\delta^{18}O_c$ compositions are much higher than the observed values, the LGM-PD differences in $\delta^{18}O_c$ are similar to the measurements. There may be two different interpretations for this discrepancy. Because our PD $\delta^{18}O_c$ values at northern high latitudes are overestimated in the simulation, it indicates colder surface temperatures than in reality. A comparably realistic decrease in surface temperature therefore introduces too cold glacial SST as compared to the reconstruction. The other way to look at this point is that either the prescribed global mean ice sheet effect in this region is underestimated, or the local isotopic decrease due to fluxes and circulation is overvalued. In this case, the $\delta^{18}O_c$ increase by the overestimated temperature decrease compensates the effect of $\delta^{18}O_w$ underestimation. Further distinct differences between model results and observations are found for the Eastern Greenland Current and polar seas, where the simulated LGM $\delta^{18}O_c$ is smaller than the observed values. In these areas, the depletion of sea surface waters by the isotopic surface fluxes and ocean circulation overwhelms the enrichment due to the global ice sheet increase, and combined with a small temperature difference, a depletion in $\delta^{18}O_c$ is simulated. In our experimental set up, river runoff is calculated by considering a closed mass balance, which means that all the precipitation falling over the Northern Hemisphere ice sheets will discharges into the Arctic Ocean. This assumption, which excludes any temporal storage of glacial precipitation on the ice sheets, may introduce unrealistic river discharge into the polar seas, leading to highly depleted waters in this region.

CPD
8, 4885–4922, 2012

5 Conclusions

In this study, we simulate the oceanic and foraminiferal calcite $\delta^{18}O$ content under LGM and PD climate conditions using the recently developed MPIOM-wiso model (Xu et al., 2012) and compare our results to available measurement reconstructions. In addition, the isotope fluxes and ocean circulation impacts on the oceanic isotope distribution are examined, respectively. Our modelled LGM $\delta^{18}O_w$ distributions present the oxygen isotope characters of the seawater in the colder and slightly weaker circulated ocean. In general, the glacial surface $\delta^{18}O_w$ distribution patterns do not show distinct differences from the present day situation, apart from larger changes in the Northern North Atlantic. The comparison between our different simulations suggests that the ice sheet impact dominates the glacial $\delta^{18}O_w$ variations from ocean surface to bottom in most regions except the northern high latitudes. In these areas, the LGM changes in topography and circulation also have an important effect on $\delta^{18}O_w$. According to the results of a sensitivity experiment (ISOPD), the variation of isotope surface fluxes mainly modifies the local isotope composition of the surface seawater, while the ocean circulation has stronger influence than the surface fluxes on the $\delta^{18}O_w$ from the subsurface to the bottom. We also simulated the present and LGM $\delta^{18}O_c$ distribution by combining sea surface temperatures and $\delta^{18}O_w$ from the model results. These $\delta^{18}O_c$ values are in good agreement with the observed $\delta^{18}O_c$ data derived from different foraminiferal species at both PD (Waelbroeck et al., 2005) and LGM (Anderson et al., 1989; Martinez et al., 1997; Kucera et al., 2005a; Meland et al., 2005), indicating an overall adequate modelled representation of the oceanic and isotopic conditions. In the tropical oceans, slightly overestimation in our simulated LGM-PD $\delta^{18}O_c$ differences as compared with the observations point to around 3 °C cooling of the SST, which is comparable to the estimation by combining different proxies (Ballantyne et al., 2005). Although the Eastern Nordic Sea in our simulation is too cold to conform to the proxy data (Kucera et al., 2005b; de Vernal et al., 2006), the agreement between the simulated and observed LGM-PD $\delta^{18}O_c$ differences in this region suggest the magnitude of

CPD
8, 4885–4922, 2012

cooling (6–8 °C) simulated in this region may be realistic. Additionally, the closed water mass balance assumption in runoff calculation will obtain impractical river discharge into the polar seas, and simulate too depleted $\delta^{18}O_c$ values at these areas.

As a logical next step, applications of oceanic and calcite oxygen isotope simulation can be used in different paleo-periods in order to obtain a mechanistic understanding of processes and to validate the models.

References

Alkama, R., Kageyama, M., Ramstein, G., Marti, O., Ribstein, P., and Swingedouw, D.: Impact of a realistic river routing in coupled ocean-atmosphere simulations of the Last Glacial Maximum climate, Clim. Dynam., 30, 855–869, doi:10.1007/s00382-007-0330-1, 2008.

Anderson, D., Prell, W., and Barratt, N.: Estimates of sea surface temperature in the Coral Sea at the last glacial maximum, Paleoceanography, 4, 615–627, 1989.

Baertschi, P.: Absolute ^{18}O content of standard mean ocean water, Earth Planet. Sc. Lett., 31, 341–344, 1976.

Ballantyne, A. P., Lavine, M., Crowley, T. J., Liu, J., and Baker, P. B.: Meta-analysis of tropical surface temperatures during the Last Glacial Maximum, Geophys. Res. Lett., 32, L05712, doi:10.1029/2004GL021217, 2005.

Barrows, T. T. and Juggins, S.: Sea-surface temperatures around the Australian margin and Indian ocean during the last glacial maximum, Quaternary Sci. Rev., 24, 1017–1047, doi:10.1016/j.quascirev.2004.07.020, 2005.

Bemis, B. E., Spero, H. J., Bijma, J., and Lea, D. W.: Reevaluation of the oxygen isotopic composition of planktonic foraminifera: experimental results and revised paleotemperature equations, Paleoceanography, 13, 150–160, 1998.

Broecker, W. S.: Oxygen isotope constraints on surface ocean temperatures, Quaternary Res., 26, 121–134, 1986.

Brovkin, V., Raddatz, T., Reick, C. H., Claussen, M., and Gayler, V.: Global biogeophysical interactions between forest and climate, Geophys. Res. Lett., 36, L07405, doi:10.1029/2009GL037543, 2009.

CPD
8, 4885–4922, 2012

Clauzet, G., Wainer, I., Lazar, A., Brady, E., and Otto-Bliesner, B.: A numerical study of the South Atlantic circulation at the Last Glacial Maximum, AAPG Stud. Geol., 253, 509–528, doi:10.1016/j.palaeo.2007.06.018, 2007.

Craig, H.: Measurement of oxygen isotope paleotemperatures, in: Stable Isotopes in Oceanographic Studies and Paleotemperatures, edited by: Tongiorgi, E., Cons. Naz. Delle. Ric, Spoleto, Italy, 161–182, 1965.

Craig, H. and Gordon, L. I.: Deuterium and oxygen 18 variations in the ocean and the marine atmosphere, in: Stable Isotopes in Oceanographic Studies and Paleotemperatures, edited by: Tongiorgi, E., Cons. Naz. di Rech., Spoleto, Italy, 9–130, 1965.

de Vernal, A., Rosell-Mele, A., Kucera, M., Hillaire-Marcel, C., Eynaud, F., Weinelt, M., Dokken, T., and Kageyama, M.: Comparing proxies for the reconstruction of LGM sea-surface conditions in the Northern North Atlantic, Quaternary Sci. Rev., 25, 2820–2834, doi:10.1016/j.palaeo.2007.06.018, 2006.

Emiliani, C.: Pleistocene temperatures, J. Geol., 538–578, 1955.

Epstein, S., Buchsbaum, R., Lowenstam, H. A., and Urey, H. C.: Revised carbonate-water isotopic temperature scale, Geol. Soc. Am. Bull., 64, 1315–1326, 1953.

Erez, J. and Luz, B.: Experimental paleotemperature equation for planktonic-foraminifera, Geochim. Cosmochim. Ac., 47, 1025–1031, 1983.

Gates, W. L., Boyle, J. S., Covey, C., Dease, C. G., Doutriaux, C. M., Drach, R. S., Fiorino, M., Gleckler, P. J., Hnilo, J. J., Marlais, S. M., Phillips, T. J., Potter, G. L., Santer, B. D., Sperber, K. R., Taylor, K. E., and Williams, D. N.: An overview of the results of the Atmospheric Model Intercomparison Project (AMIP I), B. Am. Meteorol. Soc., 80, 29–55, 1999.

Fischer, N. and Jungclaus, J. H.: Effects of orbital forcing on atmosphere and ocean heat transports in Holocene and Eemian climate simulations with a comprehensive Earth system model, Clim. Past, 6, 155–168, doi:10.5194/cp-6-155-2010, 2010.

Gersonde, R., Crosta, X., Abelmann, A., and Armand, L.: Sea-surface temperature and sea lee distribution of the Southern Ocean at the EPILOG Last Glacial Maximum – a circum-Antarctic view based on siliceous microfossil records, Quaternary Sci. Rev., 24, 869–896, doi:10.1016/j.quascirev.2004.07.015, 2005.

Hewitt, C. D., Stouffer, R. J., Broccoli, A. J., Mitchell, J. F. B., and Valdes, P. J.: The effect of ocean dynamics in a coupled GCM simulation of the Last Glacial Maximum, Clim. Dynam., 20, 203–218, doi:10.1007/s00382-002-0272-6, 2003.

CPD
8, 4885–4922, 2012

Juillet-Leclerc, A., Jouzel, J., Labeyrie, L., and Joussaume, S.: Modern and last glacial maximum sea surface $\delta^{18}O$ derived from an atmospheric general circulation model, Earth Planet. Sc. Lett., 146, 591–605, 1997.

Jungclaus, J. H., Lorenz, S. J., Timmreck, C., Reick, C. H., Brovkin, V., Six, K., Segschneider, J., Giorgetta, M. A., Crowley, T. J., Pongratz, J., Krivova, N. A., Vieira, L. E., Solanki, S. K., Klocke, D., Botzet, M., Esch, M., Gayler, V., Haak, H., Raddatz, T. J., Roeckner, E., Schnur, R., Widmann, H., Claussen, M., Stevens, B., and Marotzke, J.: Climate and carbon-cycle variability over the last millennium, Clim. Past, 6, 723–737, doi:10.5194/cp-6-723-2010, 2010.

Kitoh, A., Murakami, S., and Koide, H.: A simulation of the last glacial maximum with a coupled atmosphere-ocean GCM, Geophys. Res. Lett., 28, 2221–2224, 2001.

Knorr, G., Butzin, M., Micheels, A., and Lohmann, G.: A warm Miocene climate at low atmospheric CO_2 levels, Geophys. Res. Lett., 38, L20701, doi:10.1029/2011GL048873, 2011.

Kucera, M., Rosell-Mele, A., Schneider, R., Waelbroeck, C., and Weinelt, M.: Multiproxy approach for the reconstruction of the glacial ocean surface (MARGO), Quaternary Sci. Rev., 24, 813–819, doi:10.1016/j.quascirev.2004.07.017, 2005a.

Kucera, M., Weinelt, M., Kiefer, T., Pflaumann, U., Hayes, A., Weinelt, M., Chen, M. T., Mix, A. C., Barrows, T. T., Cortijo, E., Duprat, J., Juggins, S., and Waelbroeck, C.: Reconstruction of sea-surface temperatures from assemblages of planktonic foraminifera: multi-technique approach based on geographically constrained calibration data sets and its application to glacial Atlantic and Pacific Oceans, Quaternary Sci. Rev., 24, 951–998, doi:10.1016/j.quascirev.2004.07.014, 2005b.

LeGrande, A. N. and Schmidt, G. A.: Global gridded data set of the oxygen isotopic composition in seawater, Geophys. Res. Lett., 33, L12604, doi:10.1029/2006GL026011, 2006.

Lehmann, M. and Siegenthaler, U.: Equilibrium oxygen-isotope and hydrogen-isotope fractionation between ice and water, J. Glaciol., 37, 23–26, 1991.

Lynch-Stieglitz, J., Adkins, J. F., Curry, W. B., Dokken, T., Hall, I. R., Herguera, J. C., Hirschi, J. J. M., Ivanova, E. V., Kissel, C., Marchal, O., Marchitto, T. M., McCave, I. N., McManus, J. F., Mulitza, S., Ninnemann, U., Peeters, F., Yu, E. F., and Zahn, R.: Atlantic meridional overturning circulation during the Last Glacial Maximum, Science, 316, 66–69, doi:10.1126/science.1137127, 2007.

CPD
8, 4885–4922, 2012

Macdonald, R. W., Paton, D. W., Carmack, E. C., and Omstedt, A.: The freshwater budget and under-ice spreading of Mackenzie River water in the Canadian Beaufort Sea based on salinity and $^{18}O/^{16}O$ measurements in water and ice, J. Geophys. Res., 100, 895–919, 1995.
Majoube, M.: Fractionment en oxygéne-18 et en deuterium entre l'eau et sa vapeur, J. Chem. Phys., 10, 1423–1436, 1971.
MARGO Project Members: Constraints on the magnitude and patterns of ocean cooling at the Last Glacial Maximum, Nat. Geosci., 2, 127–132, doi:10.1038/Ngeo411, 2009.
Marsland, S. J., Haak, H., Jungclaus, J. H., Latif, M., and Roske, F.: The Max-Planck-Institute global ocean/sea ice model with orthogonal curvilinear coordinates, Ocean Model., 5, 91–127, 2003.
Martinez, J. I., DeDeckker, P., and Chivas, A. R.: New estimates for salinity changes in the Western Pacific warm pool during the Last Glacial Maximum: oxygen-isotope evidence, Mar. Micropaleontol., 32, 311–340, 1997.
Meland, M. Y., Jansen, E., and Elderfield, H.: Constraints on SST estimates for the Northern North Atlantic/Nordic Seas during the LGM, Quaternary Sci. Rev., 24, 835–852, 2005.
Mulitza, S., Boltovskoy, D., Donner, B., Meggers, H., Paul, A., and Wefer, G.: Temperature: $\delta^{18}O$ relationships of planktonic foraminifera collected from surface waters, AAPG Stud. Geol., 202, 143–152, 2003.
O'Neil, J. R., Clayton, R. N., and Mayeda, T. K.: Oxygen isotope fractionation in divalent metal carbonates, J. Chem. Phys., 51, 5547–5558, 1969.
Ortiz, J. D., Mix, A. C., Hostetler, S. W., and Kashgarian, M.: California Current of the last glacial maximum: reconstruction at 42° N based on multiple proxies, Paleoceanography, 12, 191–205, 1997.
Otto-Bliesner, B. L., Brady, E. C., Clauzet, G., Tomas, R., Levis, S., and Kothavala, Z.: Last Glacial Maximum and Holocene climate in CCSM3, J. Climate, 19, 2526–2544, 2006.
Roche, D., Paillard, D., Ganopolski, A., and Hoffmann, G.: Oceanic oxygen-18 at the present day and LGM: equilibrium simulations with a coupled climate model of intermediate complexity, Earth Planet. Sc. Lett., 218, 317–330, 2004.
Schmidt, G. A.: Forward modeling of carbonate proxy data from planktonic foraminifera using oxygen isotope tracers in a global ocean model, Paleoceanography, 14, 482–497, 1999.
Schrag, D. P., Adkins, J. F., McIntyre, K., Alexander, J. L., Hodell, D. A., Charles, C. D., and McManus, J. F.: The oxygen isotopic composition of seawater during the Last Glacial Maximum, Quaternary Sci. Rev., 21, 331–342, 2002.

CPD
8, 4885–4922, 2012

Shackleton, N. J.: Attainment of isotopic equilibrium between ocean water and the bethonic foraminifera genus *Uvigerina*: isotopic changes during the last glacial, Cent. Nat. Rech., Sci. Colloq. Int., 219, 203–209, 1974.

Shin, S. I., Liu, Z., Otto-Bliesner, B., Brady, E. C., Kutzbach, J. E., and Harrison, S. P.: A simulation of the last glacial maximum climate using the NCAR-CCSM, Clim. Dynam., 20, 127–151, doi:10.1007/s00382-002-0260-x, 2003.

Steele, M., Morley, R., and Ermold, W.: PHC: a global ocean hydrography with a high-quality Arctic Ocean, J. Climate, 14, 2079–2087, 2001.

Stepanek, C. and Lohmann, G.: Modelling mid-Pliocene climate with COSMOS, Geosci. Model Dev. Discuss., 5, 917–966, doi:10.5194/gmdd-5-917-2012, 2012.

Tindall, J., Flecker, R., Valdes, P., Schmidt, D. N., Markwick, P., and Harris, J.: Modelling the oxygen isotope distribution of ancient seawater using a coupled ocean-atmosphere GCM: implications for reconstructing early Eocene climate, Earth Planet. Sc. Lett., 292, 265–273, doi:10.1016/j.epsl.2009.12.049, 2010.

Urey, H. C.: The thermodynamic properties of isotopic substances, J. Chem. Soc., 562–581, doi:10.1039/JR9470000562, 1947.

Varma, V., Prange, M., Merkel, U., Kleinen, T., Lohmann, G., Pfeiffer, M., Renssen, H., Wagner, A., Wagner, S., and Schulz, M.: Holocene evolution of the Southern Hemisphere westerly winds in transient simulations with global climate models, Clim. Past, 8, 391–402, doi:10.5194/cp-8-391-2012, 2012.

Waelbroeck, C., Mulitza, S., Spero, H., Dokken, T., Kiefer, T., and Cortijo, E.: A global compilation of late Holocene planktonic foraminiferal δ^{18}O: relationship between surface water temperature and δ^{18}O, Quaternary Sci. Rev., 24, 853–868, 2005.

Watkins, S. J., Maher, B. A., and Bigg, G. R.: Ocean circulation at the Last Glacial Maximum: a combined modeling and magnetic proxy-based study, Paleoceanography, 22, Pa2204, doi:10.1029/2006pa001281, 2007.

Wei, W. and Lohmann, G.: Simulated Atlantic multidecadal oscillation during the Holocene, J. Climate, doi:10.1175/JCLI-D-11-00667.1, in press, 2012.

Wei, W., Lohmann, G., and Dima, M.: Distinct modes of internal variability in the global meridional overturning circulation associated to the Southern Hemisphere westerly winds, J. Phys. Oceanogr., 42, 785–801, doi:10.1175/JPO-D-11-038.1, 2012.

CPD
8, 4885–4922, 2012

Werner, M., Langebroek, P. M., Carlsen, T., Herold, M., and Lohmann, G.: Stable water isotopes in the ECHAM5 general circulation model: toward high-resolution isotope modeling on a global scale, J. Geophys. Res.-Atmos., 116, D15109, doi:10.1029/2011jd015681, 2011.

Xu, X., Werner, M., Butzin, M., and Lohmann, G.: Water isotope variations in the global ocean model MPI-OM, Geosci. Model Dev., 5, 809–818, doi:10.5194/gmd-5-809-2012, 2012.

Zachos, J. C., Stott, L. D., and Lohmann, K. C.: Evolution of early Cenozoic marine temperatures, Paleoceanography, 9, 353–387, 1994.

Zhang, X., Lohmann, G., Knorr, G., and Xu, X.: Two ocean states during the Last Glacial Maximum, Clim. Past Discuss., 8, 3015–3041, doi:10.5194/cpd-8-3015-2012, 2012.

CPD
8, 4885–4922, 2012

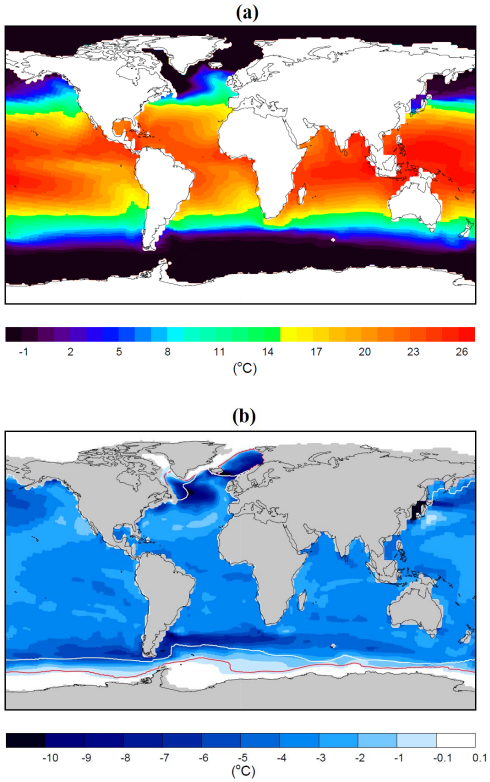

Fig. 1. (a) Modelled annual mean sea surface temperature (˚C) distribution at the LGM. **(b)** SST anomaly between LGM and PD simulations. Red line: 50 % sea ice cover at PD; white line: 50 % sea ice cover at LGM.

CPD
8, 4885–4922, 2012

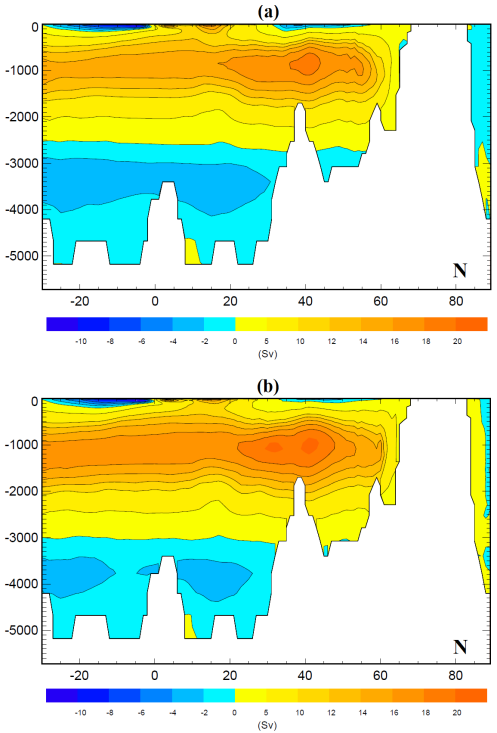

Fig. 2. (a) The Atlantic meridional ocean circulation (AMOC) in the LGM simulation. **(b)** The modelled PD AMOC. The AMOC strength is expressed in Sv ($1\,\mathrm{Sv} = 10^6\,\mathrm{m}^3\,\mathrm{s}^{-1}$).

CPD
8, 4885–4922, 2012

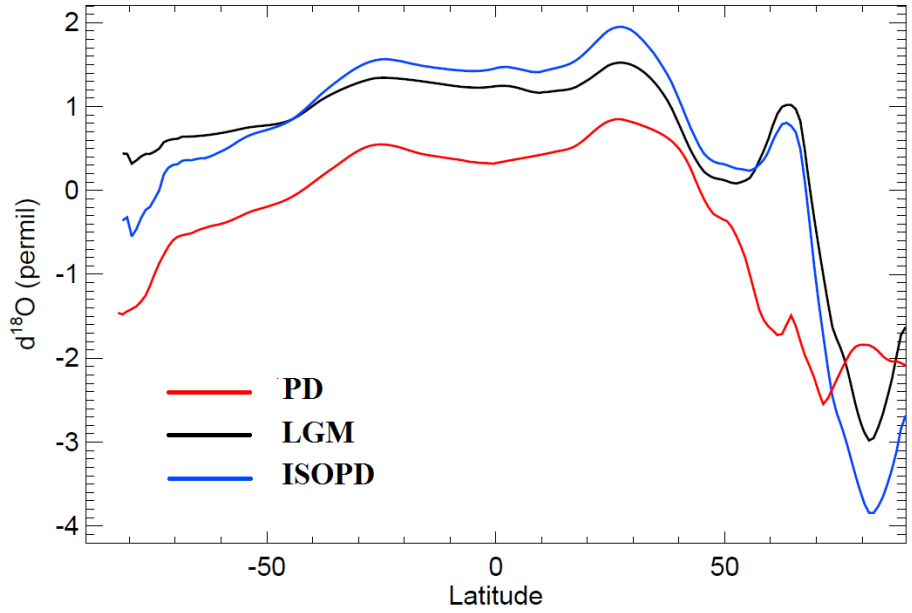

Fig. 3. The global zonal-mean $\delta^{18}O_w$ isotopic composition of sea surface water from the LGM, PD, and ISOPD simulation.

CPD
8, 4885–4922, 2012

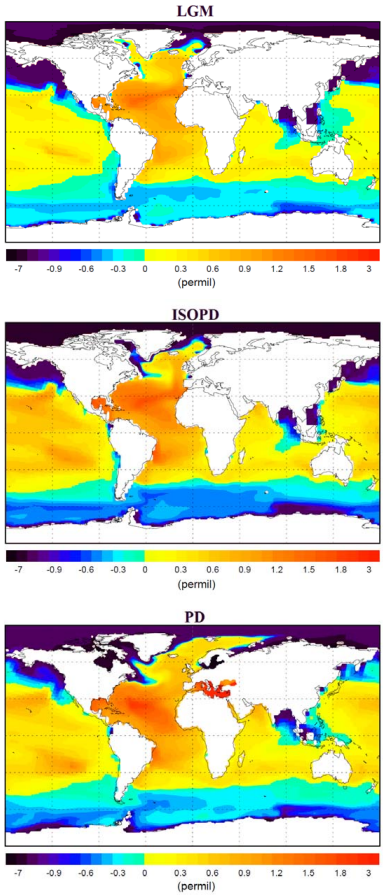

Fig. 4. Annual mean $\delta^{18}O_w$ at ocean surface modelled in the LGM, ISOPD, and PD experiments. 1 ‰ is subtracted from the LGM and ISOPD isotope values to account for the prescribed total LGM ice volume effect.

CPD
8, 4885–4922, 2012

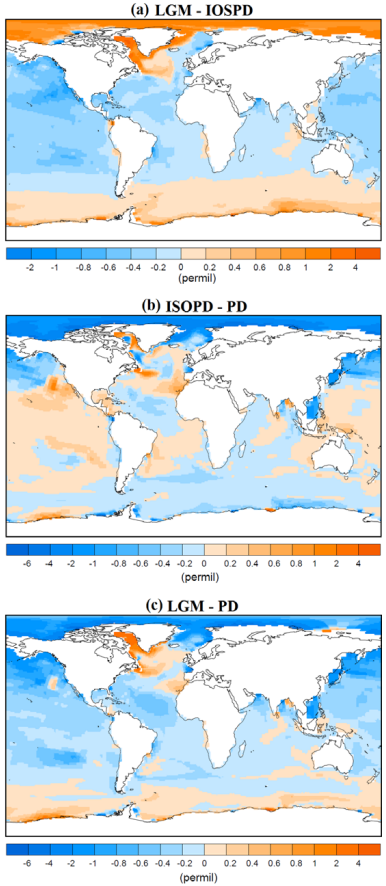

Fig. 5. The sea surface $\delta^{18}O_w$ anomalies between different model experiments (LGM, ISOPD, and PD). 1‰ is subtracted from the ISOPD-PD and LGM-PD differences to account for the prescribed total LGM ice volume effect.

CPD
8, 4885–4922, 2012

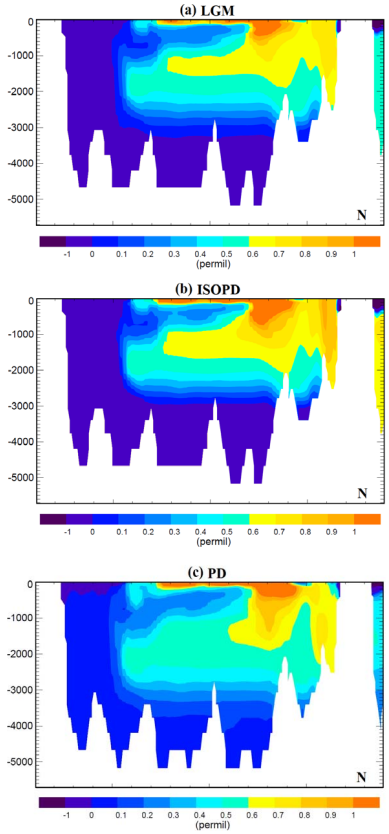

Fig. 6. The annual zonal mean $\delta^{18}O_w$ of the Atlantic basin from the LGM, ISOPD, and PD simulations. 1 ‰ is subtracted from the LGM and ISOPD isotope composition to account for the prescribed total ice volume effect.

CPD
8, 4885–4922, 2012

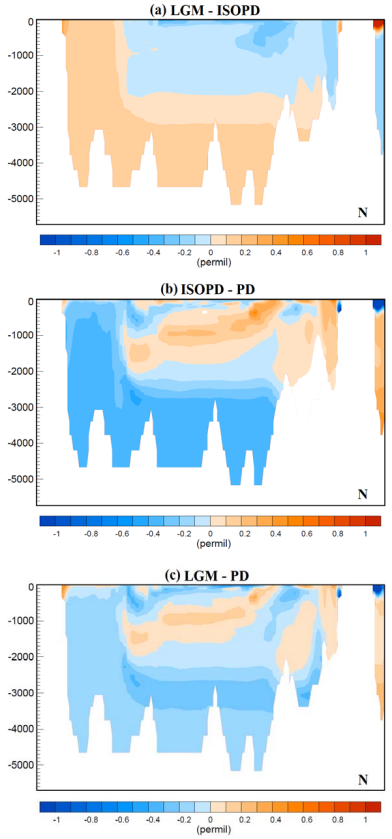

Fig. 7. The zonal mean $\delta^{18}O_w$ anomalies in the Atlantic basin between different model experiments (LGM, ISOPD, and PD). 1 ‰ is subtracted from the ISOPD-PD and LGM-PD differences to account for the prescribed total LGM ice volume effect.

CPD
8, 4885–4922, 2012

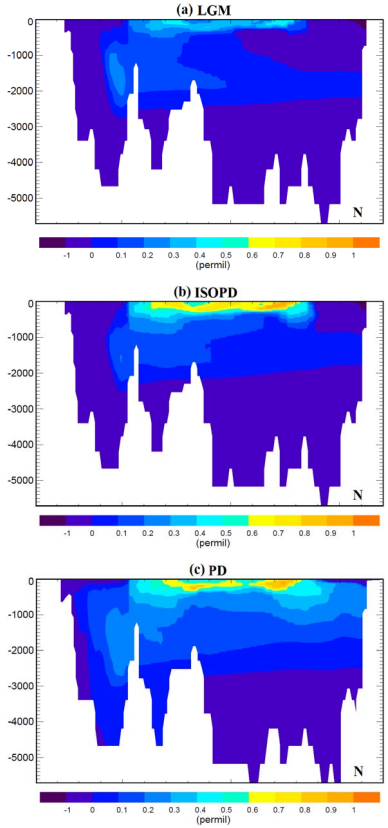

Fig. 8. The annual zonal mean $\delta^{18}O_w$ of the Pacific basin from the LGM, ISOPD, and PD simulations. 1 ‰ is subtracted from the LGM and ISOPD isotope composition to account for the prescribed total LGM ice volume effect.

CPD
8, 4885–4922, 2012

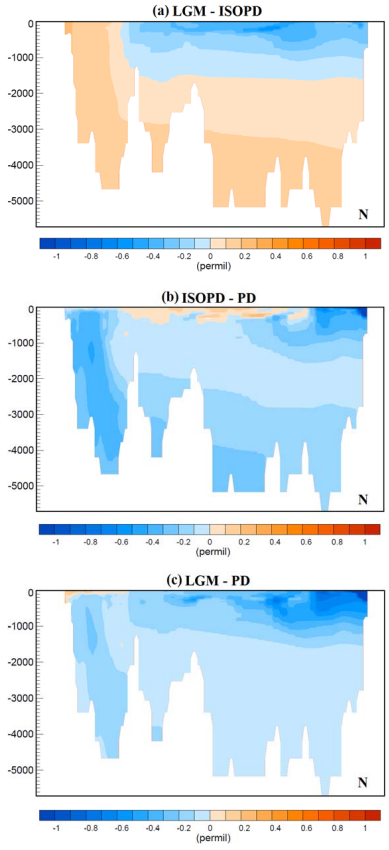

Fig. 9. The zonal mean $\delta^{18}O_w$ anomalies in the Pacific basin between different model experiments (LGM, ISOPD, and PD). 1 ‰ is subtracted from the ISOPD-PD and LGM-PD differences to account for the prescribed total LGM ice volume effect.

CPD
8, 4885–4922, 2012

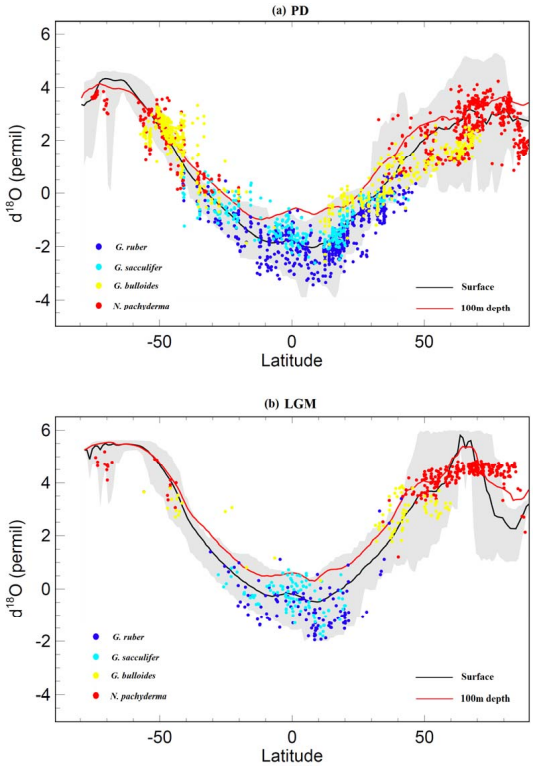

Fig. 10. Simulated zonal mean $\delta^{18}O_c$ for the ocean surface (0–10 m, black line) and bottom of the euphotic zone (~ 100 m, red line) in the PD and LGM simulations. The range of longitudinal variations in $\delta^{18}O_c$ at the ocean surface is presented as grey shading. The equation used to calculate these lines and shading is taken from Shackleton (1974). The dots indicate observational/reconstructed $\delta^{18}O_c$ data in the corresponding time period.

CPD
8, 4885–4922, 2012

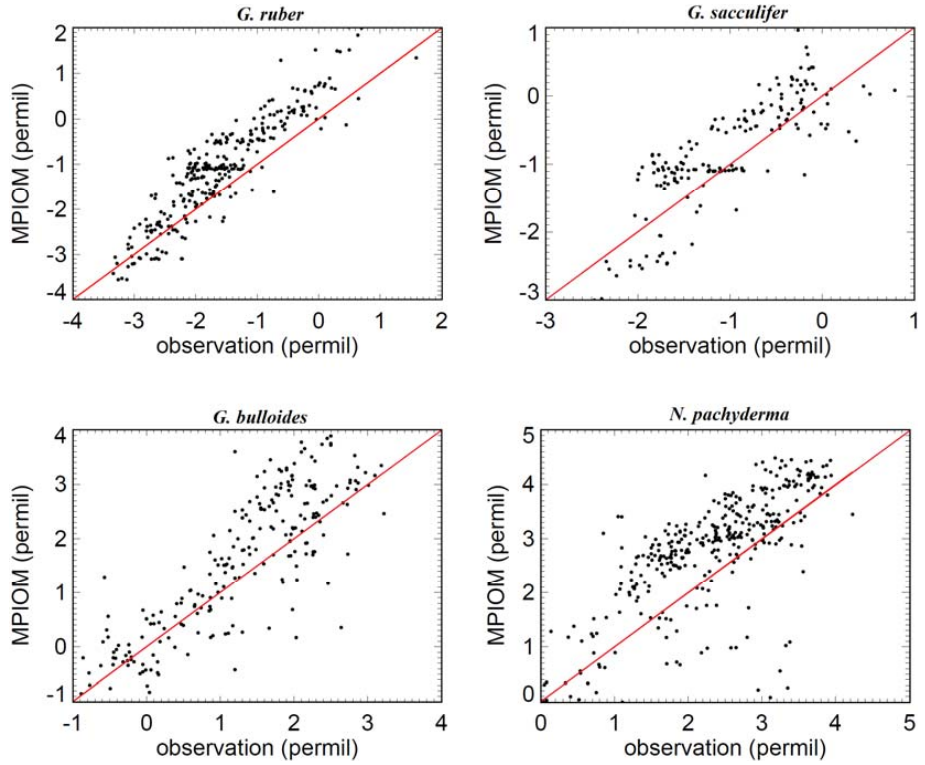

Fig. 11. Comparison of observed $\delta^{18}O_c$ showed in Fig. 10a (averaged onto the MPIOM model grid) versus modelled surface $\delta^{18}O_c$ values for the present day climate. The 1 : 1 line is colored in red.

CPD
8, 4885–4922, 2012

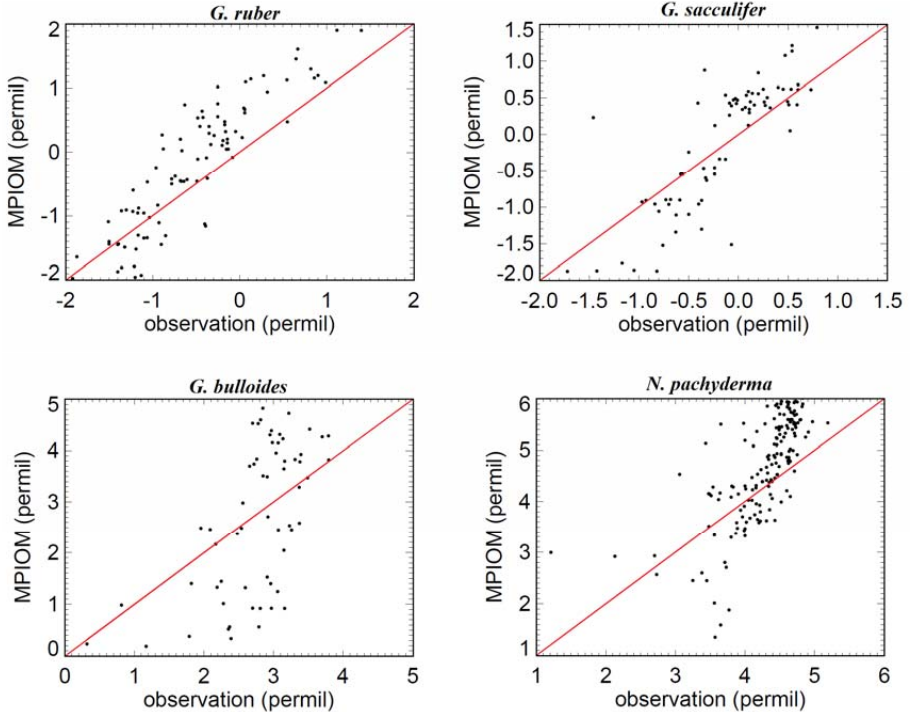

Fig. 12. Comparison of observed $\delta^{18}O_c$ showed in Fig. 10b (averaged onto the MPIOM model grid) versus modelled surface $\delta^{18}O_c$ values for the LGM climate. The 1 : 1 line is colored in red.

CPD
8, 4885–4922, 2012

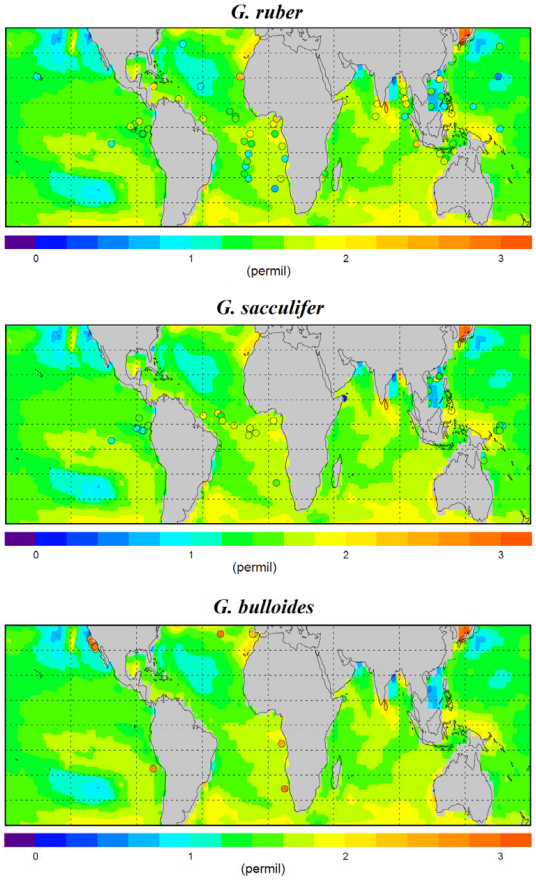

Fig. 13. Modelled $\delta^{18}O_c$ differences between LGM and PD in tropical and subtropical sea surface waters. The circles show the LGM-PD differences from the observations (*G. ruber*, *G. sacculifer*, and *G. bulloides*) where both PD and LGM measurements exist.

CPD
8, 4885–4922, 2012

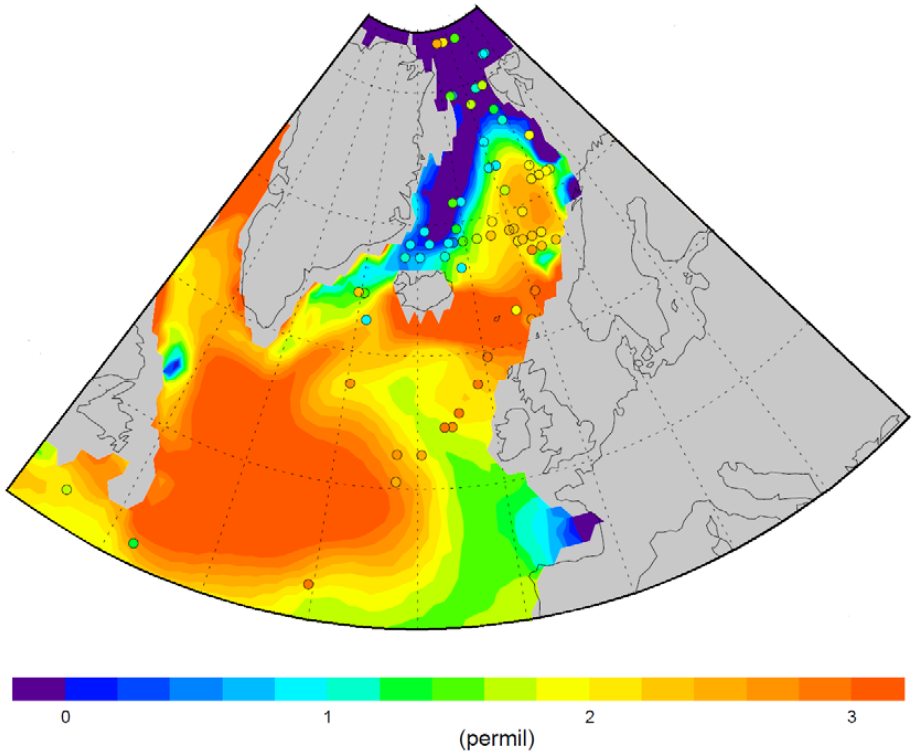

Fig. 14. Modelled $\delta^{18}O_c$ differences between LGM and PD in the North Atlantic (north of 40° N). The circles show the LGM-PD differences from the reconstructions (*N. pachyderma*) where both PD and LGM measurements exist.

CPD
8, 4885–4922, 2012